COMPUTER METHODS IN BIOMECHANICS AND BIOMEDICAL ENGINEERING, 2015
http://dx.doi.org/10.1080/10255842.2015.1075012

Taylor & Francis
Taylor & Francis Group

Effect of partial-thickness tear on loading capacities of the supraspinatus tendon: a finite element analysis

Christoph Engelhardt[a], David Ingram[b], Philippe Müllhaupt[b], Alain Farron[c], Fabio Becce[d], Dominique Pioletti[a] and Alexandre Terrier[a]

[a]Laboratory of Biomechanical Orthopaedics, EPFL, Lausanne, Switzerland; [b]Automatic Control Laboratory, EPFL, Lausanne, Switzerland; [c]Orthopaedic and Traumatology Department, CHUV, Lausanne, Switzerland; [d]Department of Diagnostic and Interventional Radiology, CHUV, Lausanne, Switzerland

ABSTRACT

Partial-thickness tears of the supraspinatus tendon frequently occur at its insertion on the greater tubercule of the humerus, causing pain and reduced strength and range of motion. The goal of this work was to quantify the loss of loading capacity due to tendon tears at the insertion area. A finite element model of the supraspinatus tendon was developed using *in vivo* magnetic resonance images data. The tendon was represented by an anisotropic hyperelastic constitutive law identified with experimental measurements. A failure criterion was proposed and calibrated with experimental data. A partial-thickness tear was gradually increased, starting from the deep articular-sided fibres. For different values of tendon tear thickness, the tendon was mechanically loaded up to failure. The numerical model predicted a loss in loading capacity of the tendon as the tear thickness progressed. Tendon failure was more likely when the tendon tear exceeded 20%. The predictions of the model were consistent with experimental studies. Partial-thickness tears below 40% tear are sufficiently stable to persist physiotherapeutic exercises. Above 60% tear surgery should be considered to restore shoulder strength.

ARTICLE HISTORY
Received 28 April 2015
Accepted 17 July 2015

KEYWORDS
Shoulder; supraspinatus tendon tear; loading capacity

1. Introduction

Active stabilization of the glenohumeral joint by the rotator cuff muscles is essential. Stability of the joint can be affected by neurological disorders, degeneration of the muscle-tendon unit or trauma. Partial-thickness tears of the rotator cuff tendons are amongst the most common causes of shoulder pathologies (Williams et al. 2004), affecting young athletes, middle-aged workers and the elderly (Herring & Nilson 1987; Fukuda et al. 1996).

Recommendations for the treatment of partial-thickness tears are still debated. Several studies have come to the conclusion that in general, surgical treatments are not always more beneficial to the patient than conservative treatments (AHRQ 2010; Seida et al. 2010). This has led to the recommendation of trying out conservative treatments first, before performing a surgery. Exceptions are severe tears, especially for young patients, where the surgical treatment should not be delayed in order to avoid irreparable rotator cuff damage (Tashjian 2012).

Amongst the rotator cuff muscles, the supraspinatus tendon is the one most often affected by tears (AAOS 2014). Tears usually manifest as a fraying of the intact tendon at the insertion site on the humeral head. In most cases, the initial partial-thickness tear, symptomatic or asymptomatic at this stage, will enlarge over time, accompanied by arising or worsening symptoms (Tempelhof et al. 1999). These symptoms include pain, reduced range of motion and decreased shoulder strength. This has been observed clinically for both symptomatic and asymptomatic supraspinatus tendon tears (McCabe et al. 2005; Kim et al. 2009). Experimental measurements of the loading capacity of supraspinatus tendons are available (Huang et al. 2005; Matsuhashi et al. 2014). Cadaveric tendons with intact insertions on the humeral head were loaded up to failure, which occurred most often at the insertional site. Partially torn tendons were however not analysed in these studies. Information on the link between partial-thickness tears and the load-bearing capabilities of the supraspinatus would contribute to improving conservative treatments. For example, physiotherapists could use this information to design exercises that are compatible with a patient's specific tendon tear.

CONTACT Alexandre Terrier alexandre.terrier@epfl.ch

Therefore, the goal of this study was to analyse the impact of partial-thickness tears on the loading capacity of the supraspinatus tendon. Assuming a nonlinear and anisotropic behaviour of the tendon, we propose a failure criterion calibrated with experimental measurements for our model. The tendon model was used in a finite element model based on magnetic resonance images (MRI) of a healthy volunteer. The loading capacities of the tendon were evaluated for progressing partial-thickness tears.

2. Methods

The used constitutive equation for the tendon model, its identification with experimental measurements and the damage criterion are introduced in the following Section 2.1. The tendon model was then applied in a patient-specific finite element analysis, built upon *in vivo* magnetic resonance imaging (Section 2.3). Failure forces were related to muscle force during arm elevation using a musculoskeletal model of the shoulder (Section 2.2).

2.1. Tendon model

2.1.1. Constitutive law

The supraspinatus tendon was modelled as an incompressible exponential hyperelastic material with one fibre family. The following strain energy potential was used (Ehret et al. 2011):

$$\Psi(\boldsymbol{C}) = \frac{\mu}{4}\left(\frac{1}{\alpha}\left[e^{\alpha(I_p-1)}-1\right]+\frac{1}{\beta}\left[e^{\beta(K-1)}-1\right]\right) \quad (1)$$

where the generalized invariants I_p and K were:

$$\begin{aligned} I_p &= \frac{w_0}{3}\mathrm{tr}(\boldsymbol{C}) + w_p\mathrm{tr}(\boldsymbol{CM}) \\ K &= \frac{w_0}{3}\mathrm{tr}\left(\boldsymbol{C}^{-1}\right) + w_p\mathrm{tr}\left(\boldsymbol{C}^{-1}\boldsymbol{M}\right) \end{aligned} \quad (2)$$

with the right Cauchy-Green strain tensor $\boldsymbol{C}$. The structural tensor $\boldsymbol{M}$ contained the information about the fibre direction $\boldsymbol{M} = \boldsymbol{m} \otimes \boldsymbol{m}$, where $\boldsymbol{m}$ is a unit vector in the fibre direction.

The first term of the invariant I_p was an isotropic term. The second term of the invariant I_p was the squared fibre stretch and thus associated with longitudinal material properties. The first term of the invariant K was an isotropic term. The second term of the invariant K was the deformation of a surface element perpendicular to the fibre direction in the reference state, and was thus associated with transverse material properties (Ehret et al. 2011).

The derivation of the strain-energy potential gave the following stress–strain relationship in terms of the second Piola-Kirchhoff stress $\boldsymbol{S}$:

$$\begin{aligned} \boldsymbol{S} = 2\frac{\partial\Psi(\boldsymbol{C})}{\partial\boldsymbol{C}} = \frac{\mu}{2}\Big\{ & e^{\alpha(I_p-1)}\left[\frac{w_0}{3}\boldsymbol{I} + w_p\boldsymbol{M}\right] \\ & -e^{\beta(K-1)}\boldsymbol{C}^{-1}\left[\frac{w_0}{3}\boldsymbol{I} + w_p\boldsymbol{M}\right]\boldsymbol{C}^{-1}\Big\} \end{aligned} \quad (3)$$

The equation contained four material parameters: μ, α, β and w_0. The lower bounds, μ, α, $\beta > 0$, ensured poly-convexity and coercivity of the constitutive law (Ball 1976). The stress-free state was associated with the reference configuration, which lead to the link between the weight factors of $w_p = 1 - w_0$ (Ehret et al. 2011).

2.1.2. Parameter identification

We identified the material parameters μ, α, β and w_0 using experimental data from human cadaveric supraspinatus tendons (Lake et al. 2009, 2010). Stress–strain curves from a slack position up to failure were available both in the longitudinal and in the transverse direction. We used Matlab's nonlinear least square algorithm lsqcurvefit to fit the nonlinear constitutive equation (Equation (3)) to the experimental data. The trust region algorithm was used because it allowed us to set lower bounds for the material parameters according to the prerequisites on strain energy functions (Section 2.1.1). The fitting was performed simultaneously in both the longitudinal and the transverse direction. We launched the least square algorithm with different randomly distributed initial values in the range of [0,100] to verify the detection of a global minimum. The root mean square error was used to assess the quality of the fit in both the longitudinal and the transverse direction with the following formula:

$$\mathrm{RMSE} = \sqrt{\frac{\sum_{i=1}^{N}\left(\sigma_i(\varepsilon_i) - \sigma^*(\varepsilon_i)\right)^2}{N}} \quad (4)$$

with the number of experimental measurement points N, the experimentally measured stress σ_i at strain ε_i, and the stress prediction of the constitutive law σ^* at the same strain.

In addition, a variance-based sensitivity analysis on the material parameters was carried out. We followed an approach based on the Monte-Carlo method (Saltelli et al. 2008, 2010). First, $2N$ random material parameter samples were generated. The material parameters were normally distributed. Mean values were the identified material parameters and the standard deviation was 1. The material parameter samples were saved in two matrices, $\mathbf{A}$ and $\mathbf{B}$, of size $N \times 4$. Further matrices $\mathbf{A}_B^i$, $1 \le i \le 4$, were generated, such that the ith column was exchanges with the ith column of matrix $\mathbf{B}$. The remaining columns were equal to matrix $\mathbf{A}$. The six matrices $\mathbf{A}$, $\mathbf{B}$ and $\mathbf{A}_B^i$ provided thus $6N$ material parameter samples. For each material parameter

sample, the stress–strain curve of the constitutive equation (Equation (3)) was evaluated. The sensitivity index S was estimated in both longitudinal and transverse direction using the formula (Saltelli et al. 2010):

$$S_i = \frac{1}{N}\sum_{j=1}^{N} \sigma_{xx}(\mathbf{B})_j \left(\sigma_{xx}\left(\mathbf{A}_B^i\right)_j - \sigma_{xx}(\mathbf{A})_j\right) \quad (5)$$

where i specified the analysed material parameter: either μ, α, β or w_0. σ was the Cauchy stress in the longitudinal (xx = 11) or transverse (xx = 22, 33) direction. The term $\sigma_{xx}(\mathbf{B})_j$ described the stress evaluated with the input parameter sample stored in the jth row of matrix $\mathbf{B}$, respectively, for matrices $\mathbf{A}$ and $\mathbf{A}_B^i$. The number of sample parameters, N, was progressively increased until the computed sensitivity indices showed convergence.

2.1.3. Damage and failure criterion

The damage and failure criterion was based on the theory of critical distances (Taylor 2007). This theory assumes that failure is preceded by the appearance of damage within a *process zone*. In this zone, energy associated with plastic deformation or micro damage is dissipated. Some loading levels can induce damage within a concentrated zone, which increases in size as loading increases until failure. At failure force, the volume of this *process zone* is by definition the critical volume (of the *process zone*). We determined this critical volume by replicating experimental measurements on the supraspinatus tendon (Huang et al. 2005) reporting a failure force of 1007 N and a nominal failure stress of 11.5 MPa. Tendon damage was assumed to occur as soon as the local maximum principal stress reaches the experimental failure stress. The volume containing stresses above the experimental failure stress was defined as *process zone*. The volume of the *process zone* under failure load was set as the critical *process zone* volume (Figure 1).

2.2. Musculoskeletal model

We used a musculoskeletal model to relate the failure force to the supraspinatus force at 90° of abduction in the scapular plane (Terrier et al. 2010; Ingram et al. 2012, 2013; Engelhardt et al. 2015). The arm elevation was simulated with a weight in the hand, starting from 0 N in steps of 10 N up to 120 N. The shoulder model was built with the MRI images of the same volunteer (Section 2.3.1). The model included thorax, clavicle, scapula and humerus. The bones were linked by spherical joints spanned by 16 muscles: subclavius, serratus anterior (3 parts), trapezius (4 parts), levator scapulae, rhomboid minor, rhomboid major (2 parts), pectoralis minor, pectoralis major (3 parts), latissimus dorsi (3 parts), deltoid (3 parts), rotator cuff (4 muscles), teres major and coracobrachialis muscles. Each muscle has been modelled with three cables, which were evenly distributed over the muscle's attachment site. A nullspace optimization algorithm coupled with inverse dynamics solved the unconstrained problem of muscle force distribution. The cost function was the sum of squared muscle stresses.

2.3. Application

2.3.1. Magnetic resonance images

A 27-year-old male volunteer showing no sign of joint abnormality was used as anatomic reference for this study. We developed a custom MRI protocol consisting of two three-dimensional T1-weighted sequences on a three Tesla MRI scanner. The first sequence was a gradient-recalled echo VIBE (TR/TE, 12.2/4.8 ms) and covered the glenohumeral joint with an isotropic resolution of 0.6 mm. The second sequence was a turbo spin-echo SPACE (TR/TE, 600/9.1 ms) and covered the whole right hemithorax with an isotropic spatial resolution of 0.9 mm. We co-registered the two sequences with Amira (FEI Visualization Sciences Group).

The supraspinatus tendon and humerus were reconstructed out of the MRI data (Figure 2). The image segmentation was performed manually using Amira. The resulting point clouds were imported into Geomagic for conversion into 3D bodies. The 3D bodies were superposed to the MRI images for visual verification. As the supraspinatus tendon merges with neighbouring tendons and the joint capsule at the lateral end, the tendon tip and its insertion are difficult to distinguish on MRI images. Therefore, a cadaveric study was additionally consulted to verify the reconstruction of this region (Curtis et al. 2006). The 3D bodies were imported into the finite element software Abaqus (Dassault Systèmes Simulia Corp., Providence, RI, USA) for stress analysis.

2.3.2. Finite element model

The constitutive equation (Equation (3)) was implemented into an user material subroutine (UMAT) in the finite element software Abaqus. To achieve an incompressible material behaviour, a penalty method was implemented (Holzapfel 2000). The UMAT implementation required the specification of the consistent elasticity tensor C. Abaqus defined C using the Jaumann derivative, which is given in incremental form by the formula:

$$\delta\boldsymbol{\sigma} = \mathbb{C} : \delta\boldsymbol{D} + \delta\boldsymbol{W}\boldsymbol{\sigma} - \boldsymbol{\sigma}\delta\boldsymbol{W} \quad (6)$$

where $\boldsymbol{\sigma}$ denoted the Cauchy stress, $\boldsymbol{D}$ was the rate of deformation tensor and $\boldsymbol{W}$ the spin tensor. $\delta\boldsymbol{D}$ and $\delta\boldsymbol{W}$ were:

$$\delta\boldsymbol{D} = \mathrm{sym}\left(\delta\boldsymbol{F}\boldsymbol{F}^{-1}\right) \quad \delta\boldsymbol{W} = \mathrm{asym}(\delta\boldsymbol{F}\boldsymbol{F}^{-1}) \quad (7)$$

with the deformation gradient $\boldsymbol{F}$.

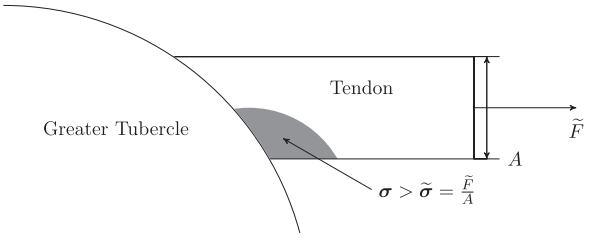

Figure 1. The critical *process zone* (grey) is defined as the volume where the stress exceeded the experimental failure stress $\tilde{\boldsymbol{\sigma}}$ associated with the failure force $\tilde{F}$. A was the cross sectional area of the tendon and $\boldsymbol{\sigma}$ the Cauchy stress.

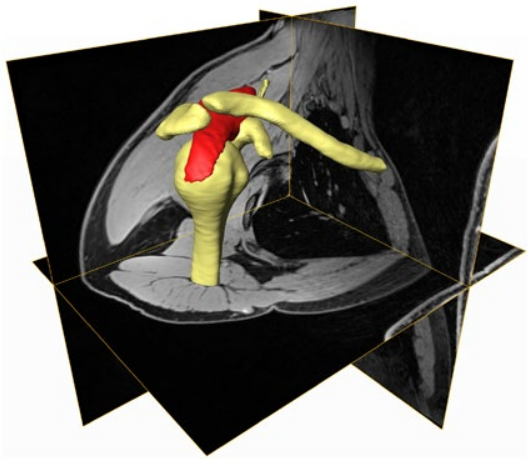

Figure 2. Reconstruction of the clavicle, scapula, humerus and supraspinatus tendon from MRI. The bones are shown in yellow and the supraspinatus muscle-tendon unit in red. Three MRI slices are shown as reference.

To calculate $\mathbb{C}$, we used a numerical approximation. We applied small perturbations on $\boldsymbol{F}$ as proposed by Miehe (1996):

$$\delta \boldsymbol{F} = \frac{\epsilon}{2}(e_i \otimes e_j \boldsymbol{F} + e_j \otimes e_i \boldsymbol{F}) \tag{8}$$

where ϵ was a perturbation parameter, which was set according to Miehe (1996). Inserting Equation (8) into Equation (7) lead to:

$$\delta \boldsymbol{D} = \frac{\epsilon}{2}(e_i \otimes e_j + e_j \otimes e_i) \quad \delta \boldsymbol{W} = 0 \tag{9}$$

The incremental change in stress was approximated by the forward difference:

$$\delta \boldsymbol{\sigma} = \boldsymbol{\sigma}(\boldsymbol{F} + \delta \boldsymbol{F}) - \boldsymbol{\sigma}(\boldsymbol{F}) \tag{10}$$

The elasticity tensor could then be approximated with the formula:

$$\mathbb{C}_{ijkl} = \frac{\boldsymbol{\sigma}(\boldsymbol{F} + \delta \boldsymbol{F})_{ij} - \boldsymbol{\sigma}(\boldsymbol{F})_{ij}}{\delta \boldsymbol{D}_{kl}} \tag{11}$$

Taking advantage of symmetry properties, it was sufficient to apply the perturbation $\delta \boldsymbol{F}$ in six directions 11, 22, 33, 12, 23, 13 to achieve all components of $\mathbb{C}$.

The tendon was attached to the humeral head at the insertion site on the greater tubercle (Curtis et al. 2006). The proximal humerus was assumed to be isotropic linear elastic. The Young's Modulus was set to 10.4 GPa and Poisson's ratio to 0.3 (Rho et al. 1993).

To simulate partial-thickness tears of the supraspinatus tendon, the insertion area between the supraspinatus tendon and the humerus was decreased. We started to decrease the insertion area from the articular-sided fibres (Figure 3), where the *process zone* appeared during the calibration simulation of the failure criterion (Section 2.1.3). A 0% tear described an intact insertion, a 50% tear indicated the insertion area was reduced by half and a 100% tear meant the complete detachment of the tendon, respectively.

The deformable parts were meshed with quadratic tetrahedral elements. The mesh size has been evaluated using the strain energy as convergence criterion.

To analyse damage and failure force, we considered a static position at 90° of arm elevation in the scapular plane. Assuming a scapulo-humeral rhythm of 2:1, the scapula was rotated by 30° and the humerus by 60° relative to the scapula. The supraspinatus muscle force applied to the tendon was increased from 0 N up to the failure force. Tendon strains were recorded and the size of the *process zone* determined.

3. Results

The identified material parameters for the constitutive law (Table 1) were independent of the initial values of the least square algorithm. The longitudinal and transverse root mean square errors were 11.24 and 1.46, respectively. The sensitivity analysis showed no interactions between the parameters ($\Sigma_i S^i = 1$). The parameter w_0 had the highest sensitivity index.

During progressive loading, the *process zone* was present at the deep articular-sided fibres at 60% of the failure force or more. As force increased, the *process zone* extended more in the longitudinal than in the transverse direction. The calibration of the tendon failure criterion lead to a critical *process zone* volume of 62 mm^3, which was set as the failure criterion for subsequent tests (Figure 4).

The failure force decreased for increasing partial-thickness tears (Figure 5). For tears between 10 and 20%, the failure force decreased less than 1%. Above 20% tear, the failure force decreased by as much as 92.5% at 90% tear. A gap appeared between the tendon tear and the bone. As force increased, the *process zone* initiated at the

Figure 3. Illustration of how tendon tears were modelled. The red part of the insertion is attached to the humerus. On the left, an intact insertion is shown, in the middle a 30% tear and on the right a 60% tear, respectively.

Table 1. Results for material parameters and corresponding sensitivity indices.

	μ	α	β	w_0
Material parameter	29.085 MPa	13.244	0.0	0.812
Sensitivity index	0.02	0.13	0.0	0.85

deep articular-side of the reduced insertion. The *process zone* then extended more in the longitudinal than in the transverse direction, until the critical volume was reached.

4. Discussion

To better understand the consequences of tears in the supraspinatus tendon, we analysed the effect of partial-thickness tears on the tendon's load bearing capability. The analysis focused on the supraspinatus's tendon insertion on the greater tubercle of the humerus. A numerical model based on MRI images of a young person was developed. We considered an anisotropic hyperelastic constitutive law, and a damage and failure criterion for the tendon. The material parameters were identified using experimental data. Partial-thickness tears of increasing size were progressively loaded until the failure criterion was reached. The predicted failure force was related to the estimated active force of the supraspinatus muscle during weight lifting.

Several constitutive laws for the tendon have already been proposed assuming hyperelastic, viscoelastic or microstructural properties (Pioletti et al. 1998; Holzapfel & Gasser 2001; Weiss et al. 2005). The constitutive law chosen for this study fulfilled the prerequisites on polyconvexity and coercivity of strain energy functions (Ball 1976; Holzapfel 2000), which are well documented (Ehret & Itskov 2007). The strain energy potential has further the advantage not to be based on additive split of isotropic and anisotropic components (Ehret et al. 2011), as other laws proposed in literature (Holzapfel et al. 2000; Balzani et al. 2006). The additive split has the disadvantage, that under compression in fibre direction, the anisotropic part has to be switched off to guarantee convexity of the strain energy potential (Ehret & Itskov 2007). This leads to an isotropic behaviour when fibres are under compression. On the other hand, a bi-linear equation might better replicate the toe region at the beginning of tendon stress–strain curves. However, our work did not focus on the transition from a tendon slack state to a loaded configuration.

Concerning the material parameter identification, we assumed that the nonlinear least square algorithm found a global minimum, since changing the initial values did not influence the result. The parameter β was the only parameter to remain on the lower bound of 0. β appears in the second term of the strain energy potential (Equation (1)) and the term vanishes as β approaches zero. Thus, the strain potential is reduced to its first term and becomes an exponential function with the invariant I_p (Equation (2)). We can thus conclude that it is sufficient to model the supraspinatus tendon using constitutive laws that consider the tissue as an isotropic matrix traversed by one fibre family. Additional terms for the transverse plane were indeed not required to match the experimental data.

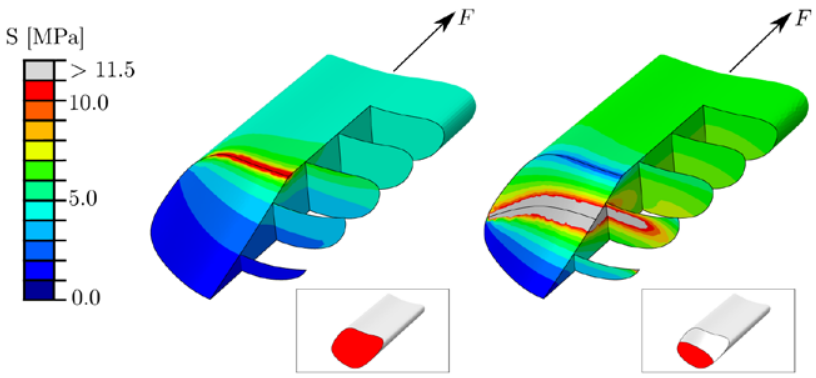

Figure 4. Stress distribution in the tendon close to its insertion on the greater tubercle of the humerus. On the left, the results for an intact insertion are shown; on the right are the results for a 50% torn tendon. Both cases are loaded with 450 N, corresponding to an abduction with 100 N in the hand. The *process zone* ($\sigma > 11.5$ MPa) is shown in grey.

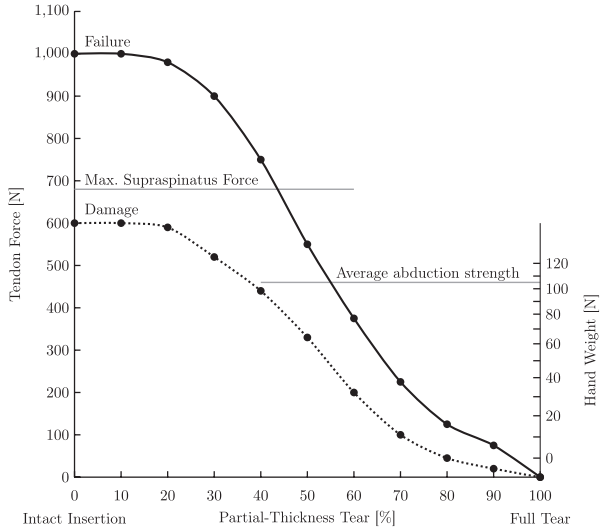

Figure 5. Failure forces for increasing tears (*process zone* volume = critical volume) and damage initiation (*process zone* volume = 10% critical volume). The forces are compared to supraspinatus forces during loaded abduction and to the theoretical maximum supraspinatus force.

The quality of the parameter identification (RMSE) was better in the transverse than in the longitudinal direction. This was related to a greater variance in the longitudinal experimental data compared to the transverse data. The sensitivity analysis proved that the parameter with the most influence was w_0. This parameter is a weight factor characterizing the relative importance of the fibre anisotropy over the isotropic matrix.

We calibrated the failure model with experimental data providing the failure stress. We chose this study because it was the only one reporting ultimate failure on complete tendons attached to the greater tubercle, while other studies used morphologically split tendons (Matsuhashi et al. 2014) or dissected tendon samples detached from bone (Lake et al. 2009, 2010). We observed however a great difference in failure stresses reported by these studies, which could be ascribed to different methods of sample preparation, testing procedure and natural property variation in biological soft tissues.

In the calibration simulation, the *process zone* initiated at the deep articular-sided aspect of tendon insertion. This is consistent with clinical observations, as well as with experimental studies reporting that tears occur most often at this site (Matsuhashi et al. 2014). The load initiating the *process zone* was dependent on the finite element mesh. This was related to the fact that loaded edges represent stress concentration points and lead to singularities in the finite element mesh where the elastic strains and stresses are theoretically infinite. However, the evolution and the final volume of the *process zone* was independent from the finite element mesh as soon as the *process zone* volume exceeded 10% of the critical volume at ultimate failure.

The critical distance approach used here to predict failure has the advantage of simplicity. It indeed only requires the elastic stress field around the stress concentration and one experimental tensile test for calibration (Taylor 2007). Although this method was initially developed for brittle materials, we justified its use in our work by the fact that stress–strain curves for tendon tissue show sudden failure without preceding plastic straining. This hypothesis has already been successfully used in micro structural (Liao & Belkoff 1999; Weiss et al. 2005) and probabilistic (De Vita & Slaughter 2007; Guo & De Vita 2009) models where brittle failure at fibre level is assumed as soon as a limit strain is exceeded. There are two alternatives of modelling failure: using cohesive element techniques, or adding damage terms in the constitutive equations. For cohesive elements, the path of crack evolution needs to be known in advance. Constitutive equations with damage terms require further experimental measurements of tissue softening at failure.

The finite element implementation of the constitutive law used a numerical approximation for the calculation of the elasticity tensor. This tensor serves as an iteration operator for the finite element solver. It thus only influences the convergence speed and not the final result (Miehe 1996). However, this approximation might lead to convergence issues when used in more complex loading cases. It might then be necessary to implement an analytical formulation of the elasticity tensor to provide stable and fast convergence.

The predicted load-bearing capacity was consistent with experimental studies on decreased abduction strength of asymptomatic and symptomatic patients with supraspinatus tendon tears (McCabe et al. 2005; Kim et al. 2009). In both studies, small and medium size tears did not significantly decrease abduction strength. However, significant deficits in abduction strength were observed for large and massive tears. In addition, the model predicts a tendency of initial tears to further expand, because the highest tissue loadings were always located at the torn side of the reduced insertion. The model further predicted arising gaps even in slight tears which would prevent self-reattachment and healing. However, the predicted forces are unlikely to be reached by patients, as increasing pain is the main limiting factor for abduction strength in patients with shoulder disorders (Kirschenbaum et al. 1993; Ben-Yishay et al. 1994; Oh et al. 2010).

The obtained supraspinatus forces lie in the range of other numerical muscle force computation algorithms (Yanagawa et al. 2008; Engelhardt et al. 2015), although some numerical studies reported supraspinatus forces to

be less than half (van der Helm 1994) or more than twice as high (Favre et al. 2012) as the results reported in this study. In either case, using optimization-based muscle force estimation risks underestimating the supraspinatus force since optimization-based methods tend to underestimate stabilizing muscle activity (Engelhardt et al. 2015). The load cases were chosen following an experimental study on the abduction strength of average middle-aged people (Kim et al. 2009), this was 102 N at the outstretched arm at 90° abduction.

Given the results of the load bearing capacity analysis, one can see that failure forces decrease following a sigmoidal function (Figure 5). The curve shows a plateau between 0 and 20% tear. Then, the slope decreases and reaches its minimum value between 40 and 60% tear. Above 60% tear, the curve flattens again. We thus assume that tear sizes between 40 and 60% represent a turning point in the evolution of tears: below 40% tear, the loading capacity stays above the theoretical maximum supraspinatus force of 688 N (Garner & Pandy 2000). Above 60%, the loading capacity dropped below the average abduction strength of 92 Nm, which corresponded to holding 10.5 kg in the hand (Kim et al. 2009).

The strength of this work is that it models the supraspinatus tendon with an anisotropic hyperelastic law identified with experimental data. The singularity associated with the tear was treated with the critical distance method, which was also calibrated with experimental data. However, stress near the insertion might be overestimated, as the model does not include the cartilaginous tissue found at the transition between bone and tendon. Although this layer is very small (Clark & Stechschulte 1998; Benjamin et al. 2006), this tissue might have a damping effect. Also, the inhomogeneity of the tendon in the transverse plane could not be included in the model due to lack of experimental data for identification of material parameters. The model could be further extended by modelling the whole supraspinatus muscle-tendon unit during movements of daily living and taking into account dynamic and fatigue failure effects.

In conclusion, we studied in a numerical analysis the reduced loading capacity of supraspinatus tendon tears. According to the numerical results, with smaller than a 40% tear, conservative treatment strategies and physiotherapy with additional weights in the hand can be considered. However, above a 60% tear, surgery should be considered to restore the loading capacities of the tendon. These results should be further investigated and confirmed by additional numerical and clinical studies. The numerical model could then be applied to patients to test further hypotheses related to rotator cuff tears. The insight into tendon mechanics will then contribute to the improvement of treatment strategies for patients.

Acknowledgements

The authors thank Caroline Sieger Fernandes for language editing and editorial assistance. This study was approved by the CIBM (Protocol number 20130328b), and complied with the principles laid down in the Declaration of Helsinki for experiments involving humans. Institutional ethics committee approval was not required for a pilot study using MRI sequences applied in routine clinical practice. Written informed consent was obtained from the volunteer.

Conflicts of Interest

No potential conflict of interest was reported by the authors.

Funding

This project was supported by the Swiss National Science Foundation [K-32K1_122512]; Fondation de soutien à la recherche dans le domaine de l'orthopédie-traumatologie; and the Centre for Biomedical Imaging (CIBM) of Lausanne University Hospital.

References

[AAOS] American Academy of Orthopaedic Surgeons. 2014. Available from: http://orthoinfo.aaos.org/topic.cfm?topic=a00064. Most tears occur in the supraspinatus muscle and tendon, … If you fall down on your outstretched arm or lift something too heavy with a jerking motion, you can tear your rotator cuff.

[AHRQ] Agency for Healthcare Research and Quality. 2010. Comparative effectiveness of nonoperative and operative treatments for rotator cuff tears. AHRQ Comparative Effectiveness Review, No. 22, Rockville, MD.

Ball JM. 1976. Convexity conditions and existence theorems in nonlinear elasticity. Arch Rational Mech Anal. 63:337–403.

Balzani D, Neff P, Schröder J, Holzapfel GA. 2006. A polyconvex framework for soft biological tissues. Adjustment to experimental data. Int J Solids Struct. 43:6052–6070.

Ben-Yishay A, Zuckerman JD, Gallagher M, Cuomo F. 1994. Pain inhibition of shoulder strength in patients with impingement syndrome. Orthopedics. 17:685–688.

Benjamin M, Toumi H, Ralphs JR, Bydder G, Best TM, Milz S. 2006. Where tendons and ligaments meet bone: attachment sites ('entheses') in relation to exercise and/or mechanical load. J Anat. 208:471–490.

Clark J, Stechschulte DJ. 1998. The interface between bone and tendon at an insertion site: a study of the quadriceps tendon insertion. J Anat. 192:605–616.

Curtis AS, Burbank KM, Tierney JJ, Scheller AD, Curran AR. 2006. The insertional footprint of the rotator cuff: an anatomic study. Arthroscopy. 22:603–609.

De Vita R, Slaughter WS. 2007. A constitutive law for the failure behavior of medial collateral ligaments. Biomech Model Mechanobiol. 6:189–197.

Ehret AE, Böl M, Itskov M. 2011. A continuum constitutive model for the active behaviour of skeletal muscle. J Mech Phys Solids. 59:625–636.

Ehret AE, Itskov M. 2007. A polyconvex hyperelastic model for fiber-reinforced materials in application to soft tissues. J Mater Sci. 42:8853–8863.

Engelhardt C, Camine VM, Ingram D, Mullhaupt P, Farron A, Pioletti D, Terrier A. 2015. Comparison of an EMG-based and a stress-based method to predict shoulder muscle forces. Comput Meth Biomech Biomed Eng. 18:1272–1279.
Favre P, Senteler M, Hipp J, Scherrer S, Gerber C, Snedeker JG. 2012. An integrated model of active glenohumeral stability. J Biomech. 45:2248–2255.
Fukuda H, Hamada K, Nakajima T, Yamada N, Tomonaga A, Goto M. 1996. Partial-thickness tears of the rotator cuff. Int Orthop. 20:257–265.
Garner BA, Pandy MG. 2000. Musculoskeletal model of the upper limb based on the visible human male dataset. Comput Methods Biomech Biomed Eng. 4:93–126.
Guo Z, De Vita R. 2009. Probabilistic constitutive law for damage in ligaments. Med Eng Phys. 31:1104–1109.
van der Helm FC. 1994. A finite element musculoskeletal model of the shoulder mechanism. J Biomech. 27:551–569.
Herring SA, Nilson KL. 1987. Introduction to overuse injuries. Clin Sports Med. 6:225–239.
Holzapfel GA. 2000. Nonlinear solid mechanics. Chichester: Wiley.
Holzapfel GA, Gasser TC. 2001. A viscoelastic model for fiber-reinforced composites at finite strains: continuum basis, computational aspects and applications. Comput Methods Appl Mech Eng. 190:4379–4403.
Holzapfel GA, Gasser TC, Ogden RW. 2000. A new constitutive framework for arterial wall mechanics and a comparative study of material models. J Elasticity. 61:1–48.
Huang C-Y, Wang VM, Pawluk RJ, Bucchieri JS, Levine WN, Bigliani LU, Mow VC, Flatow EL. 2005. Inhomogeneous mechanical behavior of the human supraspinatus tendon under uniaxial loading. J Orthop Res. 23:924–930.
Ingram D, Engelhardt C, Farron A, Terrier A, Muellhaupt P. 2013. A minimal set of coordinates for describing humanoid shoulder motion. In 2013 Ieee/Rsj International Conference on Intelligent Robots and Systems (Iros), IEEE International Conference on Intelligent Robots and Systems. Tokyo: IEEE; p. 5537–5544.
Ingram D, Müllhaupt P, Terrier A, Pralong E, Farron A. 2012. Dynamical biomechanical model of the shoulder for muscle-force estimation. Proceedings of the IEEE RAS-EMBS International Conference on Biomedical Robotics and Biomechatronics; Roma. p. 407–412.
Kim HM, Teefey SA, Zelig A, Galatz LM, Keener JD, Yamaguchi K. 2009. Shoulder strength in asymptomatic individuals with intact compared with torn rotator cuffs. J Bone Joint Surg. 91:289–296.
Kirschenbaum D, Coyle MP Jr, Leddy JP, Katsaros P, Tan F Jr, Cody RP. 1993. Shoulder strength with rotator cuff tears. Pre- and postoperative analysis. Clin Orthop Relat Res. 288:174–178.
Lake SP, Miller KS, Elliott DM, Soslowsky LJ. 2009. Effect of fiber distribution and realignment on the nonlinear and inhomogeneous mechanical properties of human supraspinatus tendon under longitudinal tensile loading. J Orthop Res. 27:1596–1602.
Lake SP, Miller KS, Elliott DM, Soslowsky LJ. 2010. Tensile properties and fiber alignment of human supraspinatus tendon in the transverse direction demonstrate inhomogeneity, nonlinearity, and regional isotropy. J Biomech. 43:727–732.
Liao H, Belkoff SM. 1999. A failure model for ligaments. J Biomech. 32:183–188.
Matsuhashi T, Hooke AW, Zhao KD, Goto A, Sperling JW, Steinmann SP, An KN. 2014. Tensile properties of a morphologically split supraspinatus tendon. Clin Anat. 27:702–706.
McCabe RA, Nicholas SJ, Montgomery KD, Finneran JJ, McHugh MP. 2005. The effect of rotator cuff tear size on shoulder strength and range of motion. J Orthop Sports Phys Ther. 35:130–135.
Miehe C. 1996. Numerical computation of algorithmic (consistent) tangent moduli in large-strain computational inelasticity. Comput Methods Appl Mech Eng. 134:223–240.
Oh JH, Yoon JP, Kim JY, Oh CH. 2010. Isokinetic muscle performance test can predict the status of rotator cuff muscle. Clin Orthop Relat Res. 468:1506–1513.
Pioletti DP, Rakotomanana LR, Benvenuti JF, Leyvraz PF. 1998. Viscoelastic constitutive law in large deformations. J Biomech. 31:753–757.
Rho JY, Ashman RB, Turner CH. 1993. Young's modulus of trabecular and cortical bone material: ultrasonic and microtensile measurements. J Biomech. 26:111–119.
Saltelli A, Annoni P, Azzini I, Campolongo F, Ratto M, Tarantola S. 2010. Variance based sensitivity analysis of model output. Design and estimator for the total sensitivity index. Comput Phys Commun. 181:259–270.
Saltelli A, Ratto M, Andres T, Campolongo F, Cariboni J, Gatelli D, Saisana M, Tarantola S. 2008. Global sensitivity analysis: the primer. Chichester: Wiley.
Seida JC, LeBlanc C, Schouten JR, Mousavi SS, Hartling L, Vandermeer B, Tjosvold L, Sheps DM. 2010. Systematic review: nonoperative and operative treatments for rotator cuff tears. Ann Intern Med. 153:246–255.
Tashjian RZ. 2012. Epidemiology, natural history, and indications for treatment of rotator cuff tears. Clin Sports Med. 31:589–604.
Taylor D. 2007. Chapter 2 – the theory of critical distances: basics: an introduction to the basic methodology of the {TCD}. In Taylor D, editor. The theory of critical distances. Oxford: Elsevier Science Ltd; p. 21–31. ISBN 978-0-08-044478-9.
Tempelhof S, Rupp S, Seil R. 1999. Age-related prevalence of rotator cuff tears in asymptomatic shoulders. J Shoulder Elbow Surg. 8:296–299.
Terrier A, Aeberhard M, Michellod Y, Mullhaupt P, Gillet D, Farron A, Pioletti D. 2010. A musculoskeletal shoulder model based on pseudo-inverse and null-space optimization. Med Eng Phys. 32:1050–1056.
Weiss JA, Gardiner JC, Ellis BJ, Lujan TJ, Phatak NS. 2005. Three-dimensional finite element modeling of ligaments: technical aspects. Med Eng Phys. 27:845–861. Advances in the finite element modelling of soft tissue deformation.
Williams GR, Rockwood CA, Bigliani LU, Iannotti JP, Stanwood W. 2004. Rotator cuff tears: why do we repair them? J Bone Joint Surg Am. 86:2764–2776.
Yanagawa T, Goodwin CJ, Shelburne KB, Giphart JE, Torry MR, Pandy MG. 2008. Contributions of the individual muscles of the shoulder to glenohumeral joint stability during abduction. J Biomech Eng. 130:021024.